Highly effective conversion of CO_2 into light olefins abundant in ethene

Sen Wang,[a,†] Li Zhang,[a,b,†] Pengfei Wang,[a,†] Xingchen Liu,[a] Zhangfeng Qin,[a] Mei Dong,[a] Jianguo Wang,[a,b] Lin He,[c,d] Unni Olsbye,[e] and Weibin Fan[a,*]

[a] *State Key Laboratory of Coal Conversion, Institute of Coal Chemistry, Chinese Academy of Sciences, P.O. Box 165, Taiyuan, Shanxi 030001, P.R. China*

[b] *University of the Chinese Academy of Sciences, Beijing 100049, P.R. China*

[c] *State Key Laboratory for Oxo Synthesis and Selective Oxidation, Suzhou Research Institute of Lanzhou Institute of Chemical Physics, Chinese Academy of Sciences, Lanzhou 730000, P.R. China*

[d] *Dalian National Laboratory for Clean Energy, Chinese Academy of Sciences, Dalian 116023, P.R. China*

[e] *Department of Chemistry, Centre for Materials and Nanoscience, SMN, University of Oslo, Blindern, NO-0315 Oslo, Norway*

[†] *These authors contributed equally to this work*

[*] *Corresponding author.* Tel.: +86-351-4199009; fax: +86-351-4041153. *E-mail address: fanwb@sxicc.ac.cn (W. Fan)*

Abstract.

Conversion of CO_2 into value-added light olefins is a potential strategy for sustainable utilization of fossil energy and biomass due to realization of carbon neutrality. However, highly selective production of light olefins, particularly of specific olefin such as ethene, from CO_2 hydrogenation is a challenge. Thus, a new catalyst system consisting of Cr_2O_3 oxide and H-SAPO-34 zeolite is manufactured here. It shows a $C_2^=$ – $C_4^=$ selectivity in hydrocarbons as high as 95.7% along with CH_4 and C_2^0 – C_4^0 selectivities of only 1.2% and 2.5% respectively at CO_2 conversion of 13.1% at 370 ºC and 0.5 MPa. More interestingly, about 74.2% of light olefins is ethene, and the ethene/propene ratio reaches 3.1, being more than 3 times of previously reported results. Such an unprecedented catalytic performance can be well maintained at least within 600 h. A combination of in situ spectroscopy, density functional theory (DFT) calculation and molecular dynamic (MD) simulation results reveals that ethanol is directly produced on Cr_2O_3 through successive hydrogenations of CH_3COO* intermediate species, which is generated through the interaction of CO_2 with CH_3* formed by dissociating the C-O bond of H_3CO* intermediate, not the insertion of CO in the H_3CO*. The produced ethanol is quickly converted into ethene on H-SAPO-34 and responsible for the primary light olefins product.

The fast consumption of fossil fuels leads to massive emission of CO_2 that causes the serious greenhouse effect and global climate change. CO_2 capture, storage and further conversion into various value-added chemicals, such as methane (CH_4), methanol (CH_3OH), formic acid (HCOOH), light olefins and aromatics, can not only reduce the CO_2 amount in atmosphere, but also develop a potential route to achieve carbon neutrality.[1–15] As an important commodity product, light olefins ($C_2^= – C_4^=$) directly converted from CO_2 has attracted many research interests.

Direct conversion of CO_2 into light olefins has been achieved via the modified Fischer−Tropsch (FT) synthesis and the formation of methanol intermediate.[16–20] Generally, the $C_2^= – C_4^=$ selectivity is lower than 61%, while the CH_4 selectivity reaches 25% in FT synthesis as a result of Anderson−Schultz−Flory (ASF) rule.[21] This is because CO_2 is firstly converted into CO via the reverse water-gas shift (RWGS) reaction, and subsequently transformed into hydrocarbons in the FT synthesis route.[22–24] To surmount the ASF rule, various metal oxides and zeolites composite catalysts have been developed as they catalytically convert CO_2 into methanol, and further into alkenes. In this way, the $C_2^= – C_4^=$ selectivity gets to 70 – 87% in hydrocarbons with a significant decrease of the CH_4 selectivity to 1 – 5% and that of $C_2^0 – C_4^0$ to 10 – 25%.[25–29]

On the other hand, control of light olefin distribution is also a challenge at a high $C_2^= – C_4^=$ selectivity. Ethene is a basic building block for many petrochemicals, and thus, has a huge market demand.[30–33] Usually, ethene is produced by steam cracking of naphtha, but it is an energy-consumption process. Therefore, development of a green and costly effective pathway to produce light olefins, particularly ethene, is of great interest, as it is scientifically

important too. Thus, direct transformation of CO_2 into ethene under mild conditions is of great interest. Recently, several Cu-based catalysts have been prepared for electrocatalytic reduction of CO_2 (CO_2 RR) into C_2 product mixture of ethene, ethanol and acetaldehyde.[34–39] However, there is a long way to go due to its very low efficiency. With respect to thermocatalytic processes, FT synthesis generally gives a ($C_2^{=}$ + C_2^{0}) selectivity ≤ 30%,[17,40–43] It also holds true for the route via formation of methanol intermediate; the ethene selectivity is not higher than 35%.[44–50] From both the practical and the theoretical viewpoints, it is imperative and necessary to manufacture a highly efficient catalyst system for hydrogenation of CO_2 to light olefins, and particularly of ethene.

In this context, a new composite catalyst consisting of Cr_2O_3 oxide and H-SAPO-34 zeolite is fabricated here for efficient conversion of CO_2 to light olefins. Interestingly, it shows a $C_2^{=}$ – $C_4^{=}$ selectivity as high as 95.7% in hydrocarbons, while the selectivity to CH_4 and that to C_2^{0} – C_4^{0} alkanes of only 1.2% and 2.5% respectively at 370 ºC and 0.5 MPa. In particular, ethene accounts for more than 74% of light olefins at CO_2 conversion of 13.1% and CO selectivity of 36.0%. As a consequence, the ethene/propene (E/P) ratio reaches 3.1, being more than three times of previously reported results (E/P ratio: ≤1.0).[44–50]

Results

Catalyst characterization. The Cr_2O_3 oxide and H-SAPO-34 zeolite were synthesized by the sol-gel and the hydrothermal methods respectively. X-ray diffraction (XRD) pattern of Cr_2O_3 oxide shows that it has a hexagonal structure (Figure 1a and 1c), as indexed to the (012), (104), (110), (113), (024), (116), (214), (030) and (220) crystal facets (JCPDS

96-900-8096). These crystal facets are further confirmed by its selected-area electron diffraction (SAED) patterns (Figure 1f). The interplanar spacing of 0.264 nm, being correspondent to the (104) crystal facet, was observed in the high-resolution transmission electron microscopy (HRTEM) image (Figure 1e). Cr_2O_3 oxide is aggregates of small nanoparticles (NPs) with a means size of 20.7 nm (Figure 1d) and a uniform and high dispersion of both Cr and O atoms (Figure 1g). Its surface area and pore volume are 60.8 m^2 g^{-1} and 0.39 cm^3 g^{-1} (Figure S1 and Table S1).

Figure S2 shows the Cr(2p) x-ray photoelectron spectra (XPS) of Cr_2O_3. Two intense peaks are observed at about 577.5 and 586.9 eV, which are assigned to $2p_{3/2}$ and $2p_{1/2}$ of Cr^{3+}.[51] The shoulder peaks around 579.9 and 589.1 eV indicate the existence of certain amounts of Cr^{6+} species.[52] These Cr^{6+} (r = 0.44 nm) species can be mostly reduced to Cr^{3+} (r = 0.62 nm) upon treatment at 400 ºC for 2 h in H_2 (Figure S2), which is supported by the shift of x-ray diffraction peaks to lower 2θ values as a result of unit cell expansion (Figure 1a, Figure S3 and Table S2). The intense peak at 531.0 eV in O(1s) XPS (Figure 1b) reveals the presence of large numbers of surface oxygen vacancies (49.3%).[53] It is supported by observing an obvious broad peak between 150 and 450 °C in the CO_2-TPD profile (Figure S4a), which is ascribed to chemically adsorbed CO_2 on surface oxygen vacancies.[8] In situ O(1s) XPS shows an increase of surface oxygen vacancy concentration after H_2 reduction (Figure 1b). This is consolidated by consuming large amounts of hydrogen between 150 and 250 ºC in the H_2-TPR profile (Figure S4b), which is indicative of the presence of more surface reducible oxygen species.[54] It needs to point out that Cr^{6+} species can be reduced to Cr^3 species, as indicated by the reduction peak between 250 and 450 °C (Figure S4b) in H_2

reduction and CO_2 hydrogenation processes,[55] but it is very difficult to be further reduced to metallic Cr, as confirmed by the in situ XPS and in situ XRD results (Figure 1a, Figure S5 and Table S3).

The prepared H-SAPO-34 samples have high crystallinity and their crystals are cuboid with a size of about 1 μm (Figure S6c). Powder mixing of it with Cr_2O_3 oxide does not influence its structure (Figure S6a). SEM and TEM images show that Cr_2O_3 NPs are dispersed on the H-SAPO-34 crystal surface (Figures S6b, S6d and S6e), as a result, leading to a slight decrease of the surface area and pore volume of H-SAPO-34 (Figure S7 and Table S4).

Catalytic evaluation. Figure 2a shows the catalytic results of Cr_2O_3/SAPO-34 composite for hydrogenation of CO_2. At 370 ºC and 0.5 MPa, $C_2^=$ – $C_4^=$ selectivity in (hydrocarbons + oxygenates) and $(C_2^= – C_4^=)/(C_2^0 – C_4^0)$ (O/P) ratio reach 96.0% and 41.8 at a moderate CO_2 conversion of 12.7% along with the selectivities to undesired CH_4 and C_2^0 – C_4^0 of just 1.0% and 2.3%, respectively. In addition, the CO selectivity is not high (32.0%). To the best of our knowledge, this light olefins selectivity is much higher than all the reported values not matter that the hydrogenation of CO_2 occurs via the Fischer−Tropsch (FT) synthesis (35 – 61%) or the methanol-intermediate (70 – 87%) route.[16–20,40–50] More interestingly, the ethene ($C_2^=$) selectivity accounts for 69.3% of light olefins (Figure 2b). This leads to a ethene/propene (E/P) ratio > 2.64, which is far higher than the results obtained on $ZnZrO_x$/SAPO-34, $ZnAl_2O_4$/SAPO-34, $ZnGa_2O_4$/SAPO-34, In_2O_3/SAPO-34 and $InZrO_x$/SAPO-34 in CO_2 hydrogenation,[44–50] where the ethene selectivity and the E/P ratio are only 20 – 35% and 0.5 – 1.0 (Figures 2c, 2d, Figure S8 and Tables S5 and S6).

Figure S9 displays the effect of reaction temperature on the catalytic performance of Cr_2O_3/SAPO-34 for conversion of CO_2 into light olefins. CO_2 conversion, as expected, increases with the reaction temperature, but the selectivity to $C_2^= - C_4^=$ and that to ethene both reach the highest value of 96.0% and 66.5% at 370 ºC and 0.5 MPa. At lower temperature of 300 ºC, CO_2 conversion, $C_2^= - C_4^=$ selectivity and ethene selectivity decrease to 6.3%, 95.1% and 57.4%, respectively. However, when the temperature is increased to 400 ºC, large amounts of CH_4, $C_2^0 - C_4^0$ and CO are generated due to enhancement of hydride transfer and RWGS reactions.[29,44–46]

The reaction pressure also has a great effect on the catalytic performance of Cr_2O_3/SAPO-34. At 370 ºC, a lower pressure of 0.25 MPa leads to a CO_2 conversion of 8.2% and a ($C_2^= - C_4^=$) selectivity of 95.3% with 65.2% of light olefins being ethene (Figure S10), while a higher pressure of 3.0 MPa decreases the $C_2^= - C_4^=$ selectivity to 76.3% while considerably increases the $C_2^0 - C_4^0$ selectivity to 18.3% owing to enhancement of light olefins hydrogenation, despite that CO_2 conversion is elevated to 21.5%. In particular, the ethene selectivity is significantly declined to 32.2%. This is probably because increases of the reaction pressure from 0.5 to 3.0 MPa promotes the formation of methanol (its selectivity raises from 37.5% to 77.9%) on Cr_2O_3 at the expense of ethanol (its selectivity drastically reduced to below 0.5%) (Figure S11).

On the basis of the above results, a new program is proposed for conducting the reaction by gradually lowering the reaction pressure. First, the reaction is carried out at 3.0 MPa. As expected, a $C_2^= - C_4^=$ selectivity of 74.5% (Figures 2e and 2f, and Figure S12), including 30.0% of ethene, 32.9% of propene and 11.6% of butene, was obtained on the

Cr_2O_3/SAPO-34. Then, a rapid reduction of the reaction pressure to 1.0 MPa raised the $C_2^=$ – $C_4^=$ selectivity to 93.6% along with a great increase in ethene selectivity to 59.5%. A more profound elevation of $C_2^=$ – $C_4^=$ selectivity to 95.7% and ethene selectivity to 71.0% was observed with a CO_2 conversion of 13.1%, when the reaction pressure was subsequently lowered to 0.5 MPa. At this condition, the E/P ratio reaches as high as 3.1.

The catalytic activity and light olefins distribution of Cr_2O_3/SAPO-34 are also related to the gas hourly space velocity (GHSV), the synthesis method of Cr_2O_3 and its integration manner with zeolite. An increase in the GHSV from 1700 to 4000 mL/(g·h) and powder mixing Cr_2O_3 and H-SAPO-34 benefit to the formation of ethene (Figures S13 and S14). Cr_2O_3(SG)/SAPO-34 shows higher CO_2 conversion than Cr_2O_3(CP)/SAPO-34, as the Cr_2O_3 prepared by the sol-gel method (designated as Cr_2O_3(SG)) has larger numbers of surface oxygen vacancies, which facilitate the adsorption and activation of CO_2, than the sample prepared by the co-precipitation method (Cr_2O_3(CP)) (Figures S15 and S16).

Catalytic stability. Cr_2O_3/SAPO-34 composite shows excellent catalytic stability in CO_2 hydrogenation to light olefins. At least within 600 h, the CO_2 conversion, $C_2^=$ – $C_4^=$ selectivity and E/P ratio are well maintained at around 8.2%, 91.0% (ethene selectivity of 62.5%) and 2.6, along with a CO selectivity of about 35.0% (Figures 3a and 3b). XRD, N_2 sorption, SEM and TEM measurements evidence that compared to the fresh catalyst, the crystal structure and the dispersion of Cr_2O_3 NPs on H-SAPO-34 of the used sample have no significant change, although the surface area and pore volume reduce due to the formation of carbonaceous species in SAPO-34 (Figures S17).

Reaction mechanism. Figure S18 displays the catalytic results obtained on pure Cr_2O_3

oxide at 370 ºC and 0.5 MPa in CO_2 hydrogenation. As expected, CH_3OH (selectivity of 37.5%) and CH_4 (selectivity of 24.1%) are the main components in (hydrocarbons + oxygenates) with a CO_2 conversion of around 5.0%. Nonetheless, appreciable amounts of ethanol (C_2H_5OH) were unexpectedly detected and its selectivity reaches 30.5% at initial stage. This suggests that the increases of the ethene selectivity on the Cr_2O_3/SAPO-34 should mainly arise from the quick conversion of the generated ethanol on Cr_2O_3 into ethene over H-SAPO-34.[56,57] Indeed, when a methanol and ethanol mixture with the same mass ratio (methanol/ethanol = 1.60/1) as that produced at initial stage over pure Cr_2O_3 oxide in CO_2 hydrogenation (Figure S18) was fed on H-SAPO-34, a selectivity to $C_2^=$ – $C_4^=$ of 96.2% with an ethene selectivity of 71.8% and an E/P ratio of 4.12 was obtained (Table S7 and Figure S19d), which are highly comparable to those attained on Cr_2O_3/SAPO-34 composite in CO_2 hydrogenation (Figures 2a and 2b). In contrast, in the methanol-to-olefins (MTO) reaction, the light olefins distribution is similar to those generally reported results with ethene, propene and butene selectivities of 25.6%, 45.7% and 18.7%, respectively (Table S7 and Figure S19a).[58–62] One may think that methylation of ethene occurs when feeding methanol and ethanol mixtures, but it is not significant, as supported by an obvious reduction in propene and butene selectivities with increasing ethanol content in the feedstock at iso-conversions (75-85%) (Table S7 and Figure S19). Difficult transformation of produced ethene into other hydrocarbons is further confirmed by the catalytic result of H-SAPO-34 for conversion of pure ethanol; ethene selectivity gets to 98.4% (Table S7 and Figure S19e).

The detailed mechanisms for formation of methanol and ethanol on Cr_2O_3 oxide were investigated by combining in situ diffuse reflectance infrared Fourier transform spectroscopy

(DRIFTS), gas chromatography−mass spectrometry (GC-MS), density functional theory (DFT) calculation and molecular dynamic simulation (MD). After being exposed to a H_2/CO_2 flow (H_2/CO_2 = 3/1, 40 mL/min) for 1 min at 300 ºC, the sample shows two board peaks in the ranges of 1470 − 1530 and 1200 − 1300 cm^{-1} (Figure 4a), which are assigned to monodentate and/or bidentate carbonate species[63,64] that are formed through adsorption of CO_2 on the surface oxygen vacancies of Cr_2O_3. Interestingly, the characteristic bands of formate species at 1592, 1562, 1354 and 1307 cm^{-1} and methoxy species between 1025 and 1090 cm^{-1} are subsequently identified, and gradually increase in the intensity with the reaction time.[65–67] This suggests that the adsorbed CO_2 on the surface oxygen vacancies quickly transform into carbonate species, and further into formate and methoxy species, which are followed by hydrogenation to methanol.[68,69] It is worth noting that the bands attributed to acetate (CH_3COO*),[70,71] acetaldehyde (CH_3CHO*)[72] and ethoxy (CH_3CH_2O*) species[73] are simultaneously observed at 1541, 1575 and 1715, and 1012 cm^{-1}, respectively (Figures 4a and 4b) in the beginning of the reaction. These species are the intermediates for formation of ethanol.

The evolution of formate, methoxy and acetate, acetaldehyde and ethoxy species with the reaction time is followed by in situ DRIFTS. The peaks for formate and methoxy species gradually intensify with prolonging reaction time, whereas those assigned to acetate, acetaldehyde and ethoxy species are enhanced up to around 20 min, and then weakened (Figures 4c and 4d), which is supported by the catalytic result that the ethanol selectivity rapidly reduces with the reaction time (Figure S18). A similar phenomenon was observed by Zhu and co-workers over Cu embedded in defect carbon.[73] Increase of the reaction

temperature from 300 to 340 and 370 °C leads to a more rapid weakening of the bands of acetate and acetaldehyde with the time on stream, along with the enhancement of the vibration bands of formate species (Figure S20).

The effluents in CO_2 hydrogenation at different reaction times are further analyzed by GC-MS spectra. Besides methanol, the ethanol is also distinctly detected on Cr_2O_3 at 370 °C and 0.5 MPa despite that its amount is much lower than that of methanol (Figures 5a, 5b, 5d and 5e). Moreover, some acetic acid species are observed at initial reaction stage, although their amount is quickly decreased with the reaction time (Figures 5c and 5f).

In contrast, no bands characteristic of acetate, acetaldehyde and ethoxy species but those of formate and methoxy species were observed in the in situ DRIFTS of $ZnZrO_x$ for CO_2 hydrogenation (Figure S21), as reported in the previous literatures.[44,74] This is further confirmed by the GC-MS analysis results that no ethanol and acetic acid species were detected during the whole reaction process in the effluents obtained on $ZnZrO_x$ at 370 °C and 0.5 MPa (Figures 5g, 5h and 5i). Thus, $ZnZrO_x$/SAPO-34 shows an ethene selectivity of 38.6%, which is similar to typical MTO results (Figure 2d).

The intrinsic reaction kinetics for formation of methanol and ethanol on Cr_2O_3 are further investigated by density functional theory (DFT) calculation. CO_2 is firstly adsorbed on the Cr_2O_3 surface oxygen vacancies, and interacts with H* to form formate (HCOO*) and methoxy (H_3CO*) species through hydrogenations (Figure 6c). Then, CH_3OH* is generated through hydrogenation of H_3CO*.[75,76] On the other hand, the H_3CO* can be dissociated into CH_3* species, and further interact with CO_2 to give acetate species (CH_3COO*). The CH_3COO* is subsequently transformed into CH_3CHO*, CH_3CH_2O* and CH_3CH_2OH*

through sequential C-O breaking and hydrogenation reactions.[77–80] The detailed optimized transition states of various steps and the calculated kinetic results are depicted in Figure 6a, 6b, Figure S22 and Table S8. The formations of HCOO* (TS2) and H_3CO* (TS6) intermediates require to overcome free energy barriers of 2.09 and 2.52 eV, with enthalpy barriers of 2.11 and 2.48 eV, and entropy losses of –0.02 and 0.04 eV, respectively, while hydrogenation of H_3CO* to CH_3OH* (TS7) just needs to surmount a free energy barrier of 1.72 eV and an enthalpy barrier of 1.60 eV, with a slight endothermic amount of 0.27 eV.

In comparison, the dissociation of C-O bond of H_3CO* to form CH_3* (TS1*) is more difficult, because its free energy barrier and enthalpy barrier reach 2.57 eV and 2.45 eV respectively. Once the CH_3* species is formed, it can rapidly interact with CO_2 to generate CH_3COO* species as results of lower free energy (1.48 eV) and enthalpy barriers (1.76 eV). Subsequently, the CH_3COO* is hydrogenated into CH_3CHO*, CH_3CH_2O* and CH_3CH_2OH* by overcoming free energy barriers of 1.76, 0.18 and 1.41 eV, with enthalpy barriers of 1.82, 0.22 and 1.39 eV, respectively (Table S8). The lower free energy barrier for the hydrogenation of H_3CO* to CH_3OH* suggests that methanol is more easily formed than ethanol on Cr_2O_3. Nevertheless, the energetic span model shows that the highest free energy surface and enthalpy surface for ethanol formation are only 1.30 and 1.74 eV respectively (Figure 6b).[81,82] In addition, formation of ethanol is thermodynamically more favorable than that of methanol (–2.36 eV vs. –1.07 eV). Thus, CO_2 hydrogenation to ethanol is feasible on Cr_2O_3, although the activity is lower than that of methanol formation.

For $ZnZrO_x$ oxide, it gives a slightly lower free energy barrier and enthalpy barrier for hydrogenation of H_3CO* than Cr_2O_3 (1.67 and 1.45 eV vs. 1.72 and 1.60 eV); however, the

free energy barrier and enthalpy barrier for the dissociation of C-O bond of H_3CO^* to form CH_3^* (3.71 eV and 3.69 eV) and the generation of CH_3COO^* via the interaction of CH_3^* with CO_2 (4.80 eV and 4.67 eV) are much higher than those on Cr_2O_3 (2.57 and 2.45 eV, and 1.48 and 1.76 eV) (Table S9). Therefore, ethanol is much more difficult to be formed on $ZnZrO_x$ than on Cr_2O_3.

It has been reported that the CH_3COO^* species is produced on Pd-Cu and Rh nano particles through insertion of CO into the C-O bond of H_3CO^* species.[77,78] However, it requires overcoming a free energy barrier and an enthalpy barrier as high as 4.00 and 3.50 eV respectively on Cr_2O_3 (Figure S23). This shows that the formation of CH_3COO^* species on Cr_2O_3 is energetically much more favorable through the interaction of CO_2 with CH_3^* formed by dissociating the C-O bond of H_3CO^* than through the insertion of CO into the C-O bond of H_3CO^* species.

Another notable point is that the free energy barrier (1.92 eV) for methane formation on Cr_2O_3 through CO dissociation and subsequent hydrogenation[83–85] is highly comparable to that for methanol formation (1.72 eV), but lower than that for ethanol formation (2.57 eV) (Tables S8 and S10). This implies that addition of CO is not good for the production of methanol and ethanol, as it would lead to formation of more CH_4 and other alkanes. Indeed, addition of CO into the feedstock ($H_2/(CO_2+CO) = 3/1$) heavily decreases the $C_2^= - C_4^=$ selectivity, and especially, the ethene selectivity, while more CH_4 and $C_2^0 - C_4^0$ are produced (Figure S24). This is consolidated by the catalytic result for CO hydrogenation; much more CH_4 and $C_2 - C_4$ hydrocarbons (including alkenes and alkanes) are produced than in CO_2 hydrogenation at the serious expense of methanol and ethanol (Figure S25).

The in situ DRIFTS shows that the peaks characteristic of formate, methoxy, acetate and acetaldehyde species in CO hydrogenation are significantly weaker than those in CO_2 hydrogenation (Figure S26). This confirms that more methanol and ethanol are formed on Cr_2O_3 in CO_2 hydrogenation than in CO hydrogenation. One might say that the CO_2 hydrogenation process generates CO through the RWGS reaction, but the overwhelming amount of CO_2 inhibits the adsorption and the dissociation of CO, as CO_2 is more strongly adsorbed on the Cr_2O_3 surface than CO (Table S11). The molecular dynamic (MD) simulation results at realistic reaction conditions (370 °C and 0.5 MPa) further corroborated this point. Although the CO_2/CO molar ratio (45/5) in the reaction mixture in the initial optimized reaction system is lower than the experimental result (95/3.5) calculated from CO_2 conversion and CO selectivity in CO_2 hydrogenation (Figure S25), the strong adsorption of CO_2 completely expels CO from approaching the surface of Cr_2O_3 (Figure S27a and Video S1). Nevertheless, when the proportion of CO_2 was decreased to the CO_2/CO molar ratio of 1/49, which is higher than the actual value (0.4/99) in CO hydrogenation (Figure S25), the Cr_2O_3 surface is almost entirely occupied by the CO (Figure S27b and Video S2). As a result, significant amounts of C_1 – C_4 hydrocarbons are produced due to the dissociation of adsorbed CO and coupling of CH_x* species.

Discussion

In summary, a new catalyst system consisting of Cr_2O_3 oxide and H-SAPO-34 zeolite has been prepared, and it shows outstanding catalytic performance for direct hydrogenation of CO_2 into light olefins at 370 ºC and 0.5 MPa; the $C_2^=$ – $C_4^=$ selectivity in hydrocarbons

reaches 95.7% with ethene accounting for 74.2% of light olefins (E/P = 3.1), but those of undesired CH_4, C_2^0 – C_4^0 and CO are only 1.2%, 2.5% and 36.0%, respectively, at CO_2 conversion of 13.1%. Such a catalytic performance can well be maintained at least within 600 h. In situ DRIFTS, GC-MS, DFT calculation and MD simulation results reveal that appreciable amount of ethanol is generated on Cr_2O_3 despite that methanol is the major product. The ethanol is formed through the interaction of CO_2 with CH_3*, which is produced by dissociating the C-O bond of H_3CO* intermediate species, and subsequent successive hydrogenations. It is then quickly converted into ethene on H-SAPO-34 molecular sieve, and thereof, leading to production of unexpectedly large amounts of light olefins with ethene as major product. This work provides not only a highly effective catalyst for conversion of CO_2 into light olefins abundant in ethene but also a new strategy for rational design of catalysts with the purpose of controlling light olefins distribution.

Methods

Catalyst preparation. Cr_2O_3 oxide was prepared by the sol-gel method. First, designed amounts of chromic nitrates ($Cr(NO_3)_3 \bullet 9H_2O$) were dissolved in 150 mL of deionized water and stirred at room temperature for 2 h. Then, the glucose was slowly added at 80 °C and vigorously stirred for at least 8 h. The obtained colloid was dried at 100 °C for 12 h, and calcined at 300 and 500 °C for 1 and 3 h respectively in air.

SAPO-34 molecular sieve was synthesized with silica sol (JN-40), phosphoric acid (H_3PO_4), pseudo-boehmite (Al_2O_3) and tetraethyl ammonium hydroxide (TEAOH). The mixture with a composition of 2.0TEAOH: 0.05SiO_2: 1.0Al_2O_3: 1.0P_2O_5: 70H_2O was stirred at room temperature for 2 h. The obtained synthesis gel was sealed into a Teflon-lined stainless steel autoclave and crystallized at 200 °C for 20 h with rotation speed of 15 rpm. The H-SAPO-34 was attained by directly calcining the as-synthesized sample at 550 °C for 10 h in air.

Catalyst characterization. Catalysts were characterized with in situ X-ray diffraction (XRD), N_2 sorption, scanning electron microscopy (SEM), transmission electron microscopy (TEM), high-resolution TEM (HRTEM), scanning transmission electron microscopy (STEM) equipped with energy-dispersive x-ray spectroscopy (EDX), in situ X-ray photoelectron spectra (XPS), temperature-programmed reduction by hydrogen (H_2-TPR), temperature programmed desorption of CO_2 (CO_2-TPD), in situ diffuse reflectance infrared Fourier transform spectra (DRIFTS) and gas chromatography−mass spectrometry (GC-MS) techniques. Details about the catalyst characterizations are described in Supplementary

Information.

DFT calculation. Periodic density functional theory (DFT) calculations within the generalized gradient approximation (GGA) were performed with the Vienna *ab initio* Simulation Package (VASP 5.3.5). The Perdew, Burke, and Ernzrhof (PBE) exchange-correlation functional was applied, and the projected augmented wave (PAW) method was employed to represent the electron−cation interactions. More information about the calculation methods are shown in Supplementary Information.

Catalytic evaluation. CO_2 conversion was carried out in a stainless steel tubular fixed-bed reactor with an inner diameter of 10 mm. 0.6 g Composite catalyst (20−40 mesh) prepared by power mixing of Cr_2O_3 oxide and H-SAPO-34 molecular sieve with a mass ratio of 1/2 was loaded unless being specifically stated. Before the reaction, the catalyst was pre-reduced at 400 ºC and atmospheric pressure for 2 h in a pure H_2 flow (30 mL/min). Then, it was cooled to 370 ºC in a N_2 flow (30 mL/min), and the CO_2 and H_2 gaseous mixture with a CO_2/H_2 of 1/3 (with 3 vol.% N_2 as internal standard) was introduced in the reactor at 370 ºC, 0.5 MPa and 4000 mL/(g·h) unless otherwise stated. The effluent products were online analyzed using an Agilent 7890A gas chromatograph (GC) equipped with one TCD and two flame ionization detectors (FID) and two capillary columns (J&W 127-7031, 30 m × 530 μm × 0.25μm; Agilent 19095P-S25, 50 m × 530 μm × 15 μm). The product selectivity (not include CO) was calculated on a molar carbon basis. The CO_2 conversion was calculated by the equation (1), and the selectivity of hydrocarbons (including alkenes and alkanes, C_nH_m) and that of oxygenates (including methanol (CH_3OH), dimethyl ether (DME) and ethanol (C_2H_5OH)) were calculated by the equations (3) and (4), respectively, without considering

CO. The CO emission was separately evaluated by the equation (2), as reported by other researchers.[44–46] Both the carbon and oxygen molar balances were ≥ 95%.

$$CO_2 \text{ conversion} = \frac{CO_{2in} - CO_{2out}}{CO_{2in}} \times 100\% \quad (1)$$

$$CO \text{ selectivity} = \frac{CO_{out}}{CO_{2in} - CO_{2out}} \times 100\% \quad (2)$$

where CO_{2in} and CO_{2out} are the inlet and outlet amounts (moles) of CO_2 respectively; CO_{out} is the outlet amount (mole) of CO.

$$C_nH_m \text{ selectivity} = n_{CnHm}/\sum(C_nH_m + \text{oxygenates}) \times 100\%; \quad (3)$$

$$\text{oxygenates selectivity} = n_{oxygenates}/\sum(C_nH_m + \text{oxygenates}) \times 100\%; \quad (4)$$

where n_{CnHm} is the carbon moles of individual hydrocarbon product at the outlet, and $\sum(C_nH_m + \text{oxygenates})$ is the total carbon moles of hydrocarbons and oxygenates. The catalytic results obtained at reaction time of 30 h were used for comparison.

Data Availability. The data that support the findings of this study including the article and its Supplementary Information are available from the corresponding authors upon a reasonable request.

References

(1) Centi, G., Quadrelli, E. A. & Perathoner, S. Catalysis for CO_2 conversion: a key technology for rapid introduction of renewable energy in the value chain of chemical industries. *Energy Environ. Sci*. **6**, 1711–1731 (2013).

(2) Porosoff, M. D. Yan, B. & Chen, J. G. Catalytic reduction of CO_2 by H_2 for synthesis of CO, methanol and hydrocarbons: challenges and opportunities. *Energy Environ. Sci*. **9**, 62–73 (2016).

(3) Alvarez, A., Bansode, A., Urakawa, A., Bavykina, A. V., Wezendonk, T. A., Makkee, M., Gascon, J. & Kapteijn, F. Challenges in the greener production of formates/formic acid, methanol, and DME by heterogeneously catalyzed CO_2 hydrogenation processes. *Chem. Rev*. **117**, 9804−9838 (2017).

(4) Wang, W., Wang, S., Ma, X. & Gong, J. Recent advances in catalytic hydrogenation of carbon dioxide. *Chem. Soc. Rev*. **40**, 3703–3727 (2011).

(5) Studt, F., Sharafutdinov, I., Abild-Pedersen, F., Elkjaer, C. F., Hummelshoj, J. S., Dahl, S., Chorkendorff, I. & Norskov, J. K. Discovery of a Ni-Ga catalyst for carbon dioxide reduction to methanol. *Nat. Chem*. **6**, 320−324 (2014).

(6) Gutterod, E. S., Lazzarini, A., Fjermestad, T., Kaur, G., Manzoli, M., Bordiga, S., Svelle, S., Lillerud, K. P., Skulason, E., Oien-Odegaard, S., Nova, A. & Olsbye, U. Hydrogenation of CO_2 to methanol by Pt nanoparticles encapsulated in UiO-67: Deciphering the role of the metal−organic framework. *J. Am. Chem. Soc*. **142**, 999−1009 (2020).

(7) Frei, M. S., Mondelli, C., Cesarini, A., Krumeich, F., Hauert, R., Stewart, J. A., Ferre, D. C. & Perez-Ramirez, J. Role of zirconia in indium oxide-catalyzed CO_2 hydrogenation to methanol. *ACS Catal*. **10**, 1133−1145 (2020).

(8) Dang, S. S., Qin, B., Yang, Y., Wang, H., Cai, J., Han, Y., Li, S. G., Gao, P. & Sun, Y. H. Rationally designed indium oxide catalysts for CO_2 hydrogenation to methanol with high activity and selectivity. *Sci. Adv*. **6**, eaaz2060 (2020).

(9) Wang, J. J., Li, G. N., Li, Z. L., Tang, C. Z., Feng, Z. C., An, H. Y., Liu, H. L., Liu, T. F. & Li, C. A highly selective and stable ZnO-ZrO_2 solid solution catalyst for CO_2 hydrogenation to methanol. *Sci. Adv*. **3**, e1701290 (2017).

(10) Wang, Y., Tan, L., Tan, M. H., Zhang, P. P., Fang, Y., Yoneyama, Y. Yang, G. H. & Tsubaki, N. Rationally designing bifunctional catalysts as an efficient strategy to boost CO_2 hydrogenation producing value-added aromatics. *ACS Catal*. **9**, 895–901 (2019).

(11) Wei, J., Ge, Q. J., Yao, R. W., Wen, Z. Y., Fang, C. Y., Guo, L. S., Xu, H. Y. & Sun, J. Directly converting CO_2 into a gasoline fuel. *Nat. Commun*. **8**, 16170 (2017).

(12) Ni, Y. M., Chen, Z. Y., Fu, Y., Liu, Y., Zhu, W. L. & Liu, Z. M. Selective conversion of CO_2 and H_2 into aromatics. *Nat. Commun*. **9**, 3457 (2018).

(13) Zhong, J. W., Yang, X. F., Wu, Z. L., Liang, B. L., Huang, Y. Q. & Zhang, T. State of the art and perspectives in heterogeneous catalysis of CO_2 hydrogenation to methanol. *Chem. Soc. Rev*. **49**, 1385–1413 (2020).

(14) Xu, Y. B., Shi, C. M., Liu, B., Wang, T., Zheng, J., Li, W. P., Liu, D. P. & Liu, X. H. Selective production of aromatics from CO_2. *Catal. Sci. Technol*. **9**, 593–610 (2019).

(15) Wang, S. W., Wu, T. J., Lin, J., Tian, J., Ji, Y. S., Pei, Y., Yan, S. R., Qiao, M. H., Xu, H. L. & Zong, B. N. FeK on 3D graphene-zeolite tandem catalyst with high efficiency and versatility in direct CO_2 conversion to aromatics. *ACS Sustainable Chem. Eng*. **7**, 17825–17833 (2019).

(16) Torres Galvis, H. M. & de Jong, K. P. Catalysts for production of lower olefins from synthesis gas: a review. *ACS Catal*. **3**, 2130–2149 (2013).

(17) Ramirez, A., Dutta Chowdhury, A., Dokania, A., Cnudde, P., Caglayan, M., Yarulina, I., Abou-Hamad, E., Gevers, L., Ould-Chikh, S., De Wispelaere, K., Van Speybroeck, V. & Gascon, J. Effect of zeolite topology and reactor configuration on the direct conversion of CO_2 to light olefins and aromatics. *ACS Catal*. **9**, 6320−6334 (2019).

(18) Wang, P., Chen, W., Chiang, F. K., Dugulan, A. L., Song, Y. J., Pestman, R., Zhang, K., Yao, J. S., Feng, B., Miao, P., Xu, W. N. & Hensen, E. J. M. Synthesis of stable and low CO_2 selective ε-iron carbide Fischer-Tropsch catalysts. *Sci. Adv*. **4**, eaau2947 (2018).

(19) Bao, J., Yang, G. H., Yoneyama, Y. & Tsubaki, N. Significant advances in C1 catalysis: highly efficient catalysts and catalytic reactions. *ACS Catal*. **9**, 3026−3053 (2019).

(20) Zhou, W., Cheng, K., Kang, J. C., Zhou, C., Subramanian, V., Zhang, Q. H. & Wang, Y. New horizon in C1 chemistry: breaking the selectivity limitation in transformation of syngas and hydrogenation of CO_2 into hydrocarbon chemicals and fuels. *Chem. Soc. Rev*. **48**, 3193−3228 (2019).

(21) Li, J., He, Y. L., Tan, L., Zhang, P. P., Peng, X. B., Oruganti, A., Yang, G. H., Abe, H., Wang, Y. & Tsubaki, N. Integrated tuneable synthesis of liquid fuels via Fischer–Tropsch technology. *Nat. Catal*. **1**, 787–793 (2018).

(22) Paalanen, P. P., Van Vreeswijk, S. H. & Weckhuysen, B. M. Combined In situ x-ray powder diffractometry/raman spectroscopy of iron carbide and carbon species evolution in Fe(-Na-S)/α-Al_2O_3 catalysts during Fischer-Tropsch synthesis. *ACS Catal*. **10**, 9837−9855 (2020).

(23) Torres Galvis, H. M. Bitter, J. H., Davidian, T., Ruitenbeek, M., Dugulan, A. I. & de Jong, K. P. Iron particle size effects for direct production of lower olefins from synthesis gas. *J. Am. Chem. Soc*. **134**, 16207–16215 (2012).

(24) Zhang, Z. P., Zhang, J., Wang, X., Si, R., Xu, J. & Han, Y. F. Promotional effects of multiwalled carbon nanotubes on iron catalysts for Fischer-Tropsch to olefins. *J. Catal*. **365**, 71–85 (2018).

(25) Jiao, F., Li, J. J., Pan, X. L., Xiao, J. P., Li, H. B., Ma, H., Wei, M. M., Pan, Y., Zhou, Z. Y., Li, M. R., Miao, S., Li, J., Zhu, Y. F., Xiao, D., He, T., Yang, J. H., Qi, F., Fu, Q. & Bao, X. H. Selective conversion of syngas to light olefins. *Science* **351**, 1065–1068 (2016).

(26) Cheng, K., Gu, B., Liu, X. L., Kang, J. C., Zhang, Q. H. & Wang, Y. Direct and highly selective conversion of synthesis gas to lower olefins: design of a bifunctional

catalyst combining methanol synthesis and carbon-carbon coupling. *Angew. Chem. Int. Ed*. **55**, 4725–4728 (2016).

(27) Jiao, F., Pan, X. L., Gong, K., Chen, Y. X., Li, G. & Bao, X. H. Shape-Selective Zeolites Promote Ethylene Formation from Syngas via a Ketene Intermediate. *Angew. Chem. Int. Ed*. **57**, 4692–4696 (2018).

(28) Zhu, Y. F. Pan, X. L., Jiao, F., Li, J., Yang, J. H., Ding, M. Z., Han, Y., Liu, Z. & Bao, X. H. Role of manganese oxide in syngas conversion to light olefins. *ACS Catal*. **7**, 2800−2804 (2017).

(29) Wang, S., Zhang, L., Zhang, W. Y., Wang, P. F., Qin, Z. F., Yan, W. J., Dong, M., Li, J. F., Wang, J. G., He, L., Olsbye, U. & Fan, W. B. Selective conversion of CO_2 into propene and butene. *Chem* **6**, 3344–3363 (2020).

(30) Ma, W. C., Xie, S. J., Liu, T. T., Fan, Q. Y., Ye, J. Y., Sun, F. F., Jiang, Z., Zhang, Q. H., Cheng, J. & Wang, Y. Electrocatalytic reduction of CO_2 to ethylene and ethanol through hydrogen-assisted C–C coupling over fluorine-modified copper. *Nat. Catal*. **3**, 478–487 (2020).

(31) Zhou, X., Wang, C., Chu, Y. Y., Xu, J., Wang, Q., Qi, G. D., Zhao, X. L. Feng, N. D. & Deng, F. Observation of an oxonium ion intermediate in ethanol dehydration to ethene on zeolite. *Nat. Commun*. **10**, 1961 (2019).

(32) Zhou, J. B., Zhi, Y. C., Zhang, J. L., Liu, Z. Q., Zhang, T., He, Y. L., Zheng, A. M., Ye, M., Wei, Y. X. & Liu, Z. M. Pre-situated ‘‘coke”-determined mechanistic route for ethene formation in the methanol-to-olefins process on SAPO-34 catalyst. *J. Catal*. **377**, 153–162 (2019).

(33) Hoang, T. T. H., Verma, S., Ma, S. C., Fister, T. T., Timoshenko, J., Frenkel, A. I., Kenis, P. J. A. & Gewirth, A. A. Nanoporous copper-silver alloys by additive-controlled electrodeposition for the selective electroreduction of CO_2 to ethylene and ethanol. *J. Am. Chem. Soc*. **140**, 5791–5797 (2018).

(34) Jiang, K., Sandberg, R. B., Akey, A. J., Liu, X.; Bell, D. C., Nørskov, J. K., Chan, K. & Wang, H. Metal ion cycling of Cu foil for selective C–C coupling in electrochemical CO_2 reduction. *Nat. Catal.* **1**, 111–119 (2018).

(35) Jung, H., Lee, S. Y., Lee, C. W., Cho, M. K., Won, D. H., Kim, C., Oh, H. S., Min, B. K. & Hwang, Y. J. Electrochemical fragmentation of Cu_2O nanoparticles enhancing selective C–C coupling from CO_2 reduction reaction. *J. Am. Chem. Soc.* **141**, 4624–4633 (2019).

(36) Zhou, Y., Che, F., Liu, M., Zou, C., Liang, Z., De Luna, P., Yuan, H., Li, J., Wang, Z., Xie, H., Li, H., Chen, P., Bladt, E., Quintero-Bermudez, R., Sham, T.-K., Bals, S., Hofkens, J., Sinton, D., Chen, G. & Sargent, E. H., Dopant-induced electron localization drives CO_2 reduction to C2 hydrocarbons. *Nat. Chem.* **10**, 974–980 (2018).

(37) Dinh, C. T., Burdyny, T., Kibria, M. G., Seifitokaldani, A., Gabardo, C. M., García de Arquer, F. P., Kiani, A., Edwards, J. P., De Luna, P., Bushuyev, O. S., Zou, C., Quintero-Bermudez, R., Pang, Y., Sinton, D. & Sargent, E. H. CO_2 electroreduction to ethylene via hydroxide-mediated copper catalysis at an abrupt interface. *Science* **360**, 783 (2018).

(38) Gao, D., Arán-Ais, R. M., Jeon, H. S. & Roldan Cuenya, B. Rational catalyst and electrolyte design for CO_2 electroreduction towards multicarbon products. *Nat. Catal*. **2**, 198–210 (2019).

(39) Zhang, B. X., Zhang, J. L., Hua, M. L., Wan, Q., Su, Z. Z., Tan, X. N., Liu, L. F., Zhang, F. Y., Chen, G., Tan, D. X., Cheng, X. Y., Han, B. X., Zheng, L. R. & Mo, G. Highly electrocatalytic ethylene production from CO_2 on nanodefective Cu nanosheets. *J. Am. Chem. Soc*. **142**, 13606–13613 (2020).

(40) Torres Galvis, H. M., Bitter, J. H., Khare, C. B., Ruitenbeek, M., Dugulan, A. I. & de Jong, K. P. Supported Iron Nanoparticles as Catalysts for Sustainable Production of Lower Olefins. *Science* **335**, 835–838 (2012).

(41) Zhong, L., Yu, F., An, Y., Zhao, Y., Sun, Y., Li, Z., Lin, T., Lin, Y., Qi, X., Dai, Y., Gu, L., Hu, J., Jin, S., Shen, Q. & Wang, H. Cobalt carbide nanoprisms for direct production of lower olefins from syngas. *Nature* **538**, 84–87 (2016).

(42) Xu, Y., Zhai, P., Deng, Y. C., Xie, J. L., Liu, X., Wang, S. & Ma, D. Highly selective olefin production from CO_2 hydrogenation on iron catalysts: A subtle synergy between manganese and sodium additives. *Angew. Chem. Int. Ed*. **59**, 21736–21744 (2020).

(43) Wang, X., Wu, D. K., Zhang, J. L., Gao, X. H., Ma, Q. X., Fan, S. B. & Zhao, T. S. Highly selective conversion of CO_2 to light olefins via Fischer-Tropsch synthesis over stable layered K–Fe–Ti catalysts. *Appl. Catal. A.* **573**, 32–40 (2019).

(44) Li, Z. L., Wang, J. J., Qu, Y. Z., Liu, H. L., Tang, C. Z., Miao, S., Feng, Z. C., An, H. Y. & Li, C. Highly selective conversion of carbon dioxide to lower olefins. *ACS Catal*. **7**, 8544−8548 (2017).

(45) Gao, P., Dang, S. S., Li, S. G., Bu, X. N., Liu, Z. Y., Qiu, M. H., Yang, C. G., Wang, H., Zhong, L. S., Han, Y., Liu, Q., Wei, W. & Sun, Y. H. Direct production of lower olefins from CO_2 conversion via bifunctional catalysis. *ACS Catal*. **8**, 571−578 (2018).

(46) Liu, X. L., Wang, M. H., Zhou, C., Zhou, W., Cheng, K., Kang, J. C., Zhang, Q. H., Deng, W. P. & Wang, Y. Selective transformation of carbon dioxide into lower olefins with a bifunctional catalyst composed of $ZnGa_2O_4$ and SAPO-34. *Chem. Commun*. **54**,140−143 (2018).

(47) Numpilai, T., Wattanakit, C., Chareonpanich M. & Limtrakul, J. Optimization of synthesis condition for CO_2 hydrogenation to light olefins over In_2O_3 admixed with SAPO-34. *Energ. Convers. Manage*. **180**, 511–523 (2019).

(48) Dang, S. S., Gao, P., Liu, Z. Y., Chen, X. Q., Yang, C. G., Wang, H., Zhong, L. S., Li, S. G. & Sun, Y. H. Role of zirconium in direct CO_2 hydrogenation to lower olefins on oxide/zeolite bifunctional catalysts. *J. Catal*. **364**, 382–393 (2018).

(49) Gao, J. J., Jia, C. M. & Liu, B. Direct and selective hydrogenation of CO_2 to ethylene and propene by bifunctional catalysts. *Catal. Sci. Technol*. **7**, 5602–5607 (2017).

(50) Liu, X. L., Wang, M. H., Yin, H. R., Hu, J. T., Cheng, K., Kang, J. C., Zhang, Q. H. & Wang, Y. Tandem catalysis for hydrogenation of CO and CO_2 to lower olefins with bifunctional catalysts composed of spinel oxide and SAPO-34. *ACS Catal*. **10**, 8303−8314 (2020).

(51) Hosseini, S. A., Alvarez-Galvan, M. C., Fierro, J. L. G., Niaei, A. & Salari, D. MCr_2O_4 (M=Co, Cu, and Zn) nanospinels for 2-propanol combustion: Correlation of structural properties with catalytic performance and stability. *Ceramics International* **39**, 9253–9261 (2013).

(52) Gao, X. F., Wu, Y. Q., Zhang, T., Wang, L. Y., Li, X. L., Xie, H. J. & Tan, Y. S. Binary ZnO/Zn–Cr nanospinel catalysts prepared by a hydrothermal method for isobutanol synthesis from syngas. *Catal. Sci. Technol*. **8**, 2975–2986 (2018).

(53) Zhang, Z. X., Wang, Y. H., Lu, J. M., Zhang, J., Li, M. R., Liu, X. B. & Wang, F. Pr-doped CeO_2 catalyst in the prins condensation-hydrolysis reaction: are all of the defect sites catalytically active? *ACS Catal*. **8**, 2635−2644 (2018).

(54) Piumetti, M., Bensaid, S., Russo, N. & Fino, D. Nanostructured ceria-based catalysts for soot combustion: investigations on the surface sensitivity. *Appl. Catal. B* 165, 742–751 (2015).

(55) Kanervo, J. M. & Krause, A. O. I. Characterisation of Supported Chromium Oxide Catalysts by Kinetic Analysis of H_2-TPR Data. *J. Catal*. **207**, 57–65 (2002).

(56) Masih, D., Rohani, S., Kondo, J. N. & Tatsumi, T. Catalytic dehydration of ethanol-to-ethylene over Rho zeolite under mild reaction conditions. *Microporous Mesoporous Mater*. **282**, 91–99 (2019).

(57) Li, X., Rezaei, F., Ludlow, D. K. & Rownaghi, A. A. Synthesis of SAPO-34@ZSM-5 and SAPO-34@Silicalite-1 Core−Shell Zeolite Composites for Ethanol Dehydration. *Ind. Eng. Chem. Res*. **57**, 1446−1453 (2018).

(58) Hereijgers, B. P. C., Bleken, F., Nilsen, M. H., Svelle, S., Lillerud, K. P., Bjorgen, M., Weckhuysen, B. M. & Olsbye, U. Product shape selectivity dominates the Methanol-to-Olefins (MTO) reaction over H-SAPO-34 catalysts. *J. Catal*. **264**, 77–87 (2009).

(59) Li, J. F., Wei, Z. H., Chen, Y. Y., Jing, B. Q., He, Y., Dong, M., Jiao, H. J., Li, X. K., Qin, Z. F., Wang, J. G. & Fan, W. B. A route to form initial hydrocarbon pool species in methanol conversion to olefins over zeolites. *J. Catal*. **317**, 277–283 (2014).

(60) Li, J. Z., Wei, Y. X., Liu, G. Y., Qi, Y., Tian, P., Li, B., He, Y. L. & Liu, Z. M. Comparative study of MTO conversion over SAPO-34, H-ZSM-5 and H-ZSM-22: Correlating catalytic performance and reaction mechanism to zeolite topology. *Catal. Today* **171**, 221–228 (2011).

(61) Gao, S. S., Xu, S. T., Wei, Y. X., Qiao, Q. L., Xu, Z. C., Wu, X. Q., Zhang, M. Z., He, Y. L., Xu, S. L. & Liu, Z. M. Insight into the deactivation mode of methanol-to-olefins conversion over SAPO-34: Coke, diffusion, and acidic site accessibility. *J. Catal*. **367**, 306–314 (2018).

(62) Dai, W. L., Wang, X., Wu, G. J., Guan, N. J., Hunger, M. & Li, L. D. Methanol-to-Olefin Conversion on Silicoaluminophosphate Catalysts: Effect of Brønsted Acid Sites and Framework Structures. *ACS Catal*. **1**, 292–299 (2011).

(63) Yao, L. B., Shen, X. C., Pan, Y. B. & Peng, Z. M. Synergy between active sites of Cu-In-Zr-O catalyst in CO_2 hydrogenation to methanol. *J. Catal*. **372**, 74–85 (2019).

(64) Wang, Y. H., Kattel, S., Gao, W. G., Li, K. Z., Liu, P., Chen, J. G. G. & Wang, H. Exploring the ternary interactions in Cu-ZnO-ZrO_2 catalysts for efficient CO_2 hydrogenation to methanol. *Nat. Commun*. **10**, 1166 (2019).

(65) Yan, B. H., Zhao, B. H., Kattel, S., Wu, Q. Y., Yao, S. Y., Su, D. & Chen, J. G. G. Tuning CO_2 hydrogenation selectivity via metal-oxide interfacial sites. *J. Catal*. **374**, 60–71 (2019).

(66) Feng, O. Y., Kondo, J. N., Maruya, K. & Domen, K. Site conversion of methoxy species on ZrO_2. *J. Phys. Chem. B* **101**, 4867–4869 (1997).

(67) Kattel, S., Yan, B., Yang, Y., Chen, J. G. & Liu, P. Optimizing binding energies of key intermediates for CO_2 hydrogenation to methanol over oxide-supported copper. *J. Am. Chem. Soc*. **138**, 12440–12450 (2016).

(68) Jiang, X., Nie, X. W., Wang, X. X., Wang, H. Z., Koizumi, N., Chen, Y. G., Guo, X. W. & Song, C. S. Origin of Pd-Cu bimetallic effect for synergetic promotion of methanol formation from CO_2 hydrogenation. *J. Catal*. **369**, 21–32 (2019).

(69) Zhang, L., Mao, F. X., Zheng, L. R., Wang, H. F., Yang, X. H. & Yang, H. G. Tuning Metal Catalyst with Metal−C_3N_4 Interaction for Efficient CO_2 Electroreduction. *ACS Catal*. **8**, 11035−11041 (2018).

(70) Wang, L. X., He, S. X., Wang, L., Lei, Y., Meng, X. J. & Xiao, F. S. Cobalt−Nickel Catalysts for Selective Hydrogenation of Carbon Dioxide into Ethanol. *ACS Catal*. **9**, 11335−11340 (2019).

(71) Wang, L. X., Wang, L., Zhang, J. Liu, X. L., Wang, H., Zhang, W., Yang, Q., Ma, J. Y., Dong, X., Yoo, S. J., Kim, J. G., Meng, X. J. & Xiao, F. S. Selective hydrogenation of CO_2 to ethanol over cobalt catalysts. *Angew. Chem. Int. Ed*. **57**, 1–6 (2018).

(72) Xu, D., Ding, M. Y., Hong, X. L., Liu, G. L. & Tsang, S. C. E. Selective C_{2+} Alcohol Synthesis from Direct CO_2 Hydrogenation over a Cs-Promoted Cu-Fe-Zn Catalyst. *ACS Catal*. **10**, 5250−5260 (2020).

(73) Li, S. H., Saranya, G., Chen, M. Y. & Zhu, Y. Selectivity switch in transformation of CO_2 from ethanol to methanol on Cu embedded in the defect carbon. *Sci China Chem* **63**, 722–730 (2020).

(74) Liu, X. L., Zhou, W., Yang, Y. D., Cheng, K., Kang, J. C., Zhang, L., Zhang, G. G., Min, X. J., Zhang, Q. H. & Wang, Y. Design of efficient bifunctional catalysts for direct conversion of syngas into lower olefins via methanol/dimethyl ether intermediates. *Chem. Sci*. **9**, 4708–4718 (2018).

(75) Choi, H., Oh, S. Y., Tran, S. B. T. & Park, J. Y. Size-controlled model Ni catalysts on Ga_2O_3 for CO_2 hydrogenation to methanol. *J. Catal*. **376**, 68–76 (2019).

(76) Peng, Y. H., Wang, L. B., Luo, Q. Q., Gao, Y., Dai, Y. Z., Li, Z. L., Li, H. L., Zheng, X. S., Yan, W. S., Yang, J. L. & Zeng, J. Molecular-level insight into how hydroxyl groups boost catalytic activity in CO_2 hydrogenation into methanol. *Chem* **4**, 613–625 (2018).

(77) Bai, S. X., Shao, Q., Wang, P. T., Dai, Q. G., Wang, X. Y. & Huang, X. Q. Highly Active and Selective Hydrogenation of CO_2 to Ethanol by Ordered Pd−Cu Nanoparticles. *J. Am. Chem. Soc*. **139**, 6827−6830 (2017).

(78) Choi, Y. M. & Liu, P. Mechanism of Ethanol Synthesis from Syngas on Rh(111). *J. Am. Chem. Soc*. **131**, 13054–13061 (2009).

(79) He, Z. H., Qian, Q. L., Ma, J., Meng, Q. L., Zhou, H. C., Song, J. L., Liu, Z. M. & Han, B. X. Water-enhanced synthesis of higher alcohols from CO_2 hydrogenation over a Pt/Co_3O_4 catalyst under milder conditions. *Angew. Chem. Int. Ed*. **55**, 737–741 (2016).

(80) An, B., Li, Z., Song, Y., Zhang, J. Z., Zeng, L. Z., Wang, C. & Lin, W. B. Cooperative copper centres in a metal-organic framework for selective conversion of CO_2 to ethanol. *Nat. Catal*. **2**, 709–717 (2019).

(81) Kozuch, S. & Shaik, S. How to conceptualize catalytic cycles? The energetic span model. *Acc. Chem. Res*. **44**, 101–110 (2011).

(82) Wang, C. M., Wang, Y. D., Du, Y. J., Yang, G. & Xie, Z. K. Similarities and differences between aromatic-based and olefin-based cycles in H-SAPO-34 and H-SSZ-13 for methanol-to-olefins conversion: Insights from energetic span model. *Catal. Sci. Technol*. **5**, 4354–4364 (2015).

(83) Ronsch, S., Schneider, J., Matthischke, S., Schluter, M., Gotz, M., Lefebvre, J., Prabhakaran, P. & Bajohr, S. Review on methanation-From fundamentals to current projects. *Fuel* **166**, 276–296 (2016).

(84) Zhang, R. G., Wang, G. R. & Wang, B. J. Insights into the mechanism of ethanol formation from syngas on Cu and an expanded prediction of improved Cu-based catalyst. *J. Catal*. **305**, 238–255 (2013).

(85) Ren, J., Guo, H. L., Yang, J. Z., Qin, Z. F., Lin, J. Y. & Li, Z. Insights into the mechanisms of CO_2 methanation on Ni(111) surfaces by density functional theory. *Appl. Surf. Sci*. **351**, 504–516 (2015).

Acknowledgements

The authors are grateful to the financial supports of the National Key R&D Program of China (2018YFB0604802; 2020YFB0606402), National Natural Science Foundation of China (U1910203; U1862101; 21991092; 21802157; 21875275; 201603254), Strategic Priority Research Program of the Chinese Academy of Sciences (CAS) (XDA21020500), Natural Science Foundation of Shanxi Province of China (201901D211581), Youth Innovation Promotion Association CAS (2021172), Autonomous research project of State Key Laboratory of Coal Conversion, Institute of Coal Chemistry, CAS (2020BWZ004), Young

Talent Training Program of State Key Laboratory of Coal Conversion, Institute of Coal Chemistry, CAS (2021BWZ003), Excellent doctoral student award and subsidy program of Shanxi Province (BK2018001), East-West Cooperation Project of Ningxia Key R & D Plan (2017BY063), the Dalian National Laboratory for Clean Energy (DNL) Cooperation Fund, the CAS (DNL201919), and the European Union's Horizon 2020 research and innovation program under grant agreement no 837733. The calculations were performed in the Computer Network Information Center of CAS and the National Supercomputer Centers in Lvliang of China.

Author contributions

S.W., L.Z., P.W. implemented the experiments including catalyst preparation, characterization, catalytic reaction and theoretical calculation; S.W. wrote the paper; X.L., Z.Q., M.D. carried out part of catalytic tests as well as some catalyst characterization; J.W., L.H., U.O. gave fruitful discussions on the reaction mechanism; W.F. conceived the whole project, guided the work and revised the paper. S.W., L.Z., P.W., contributed equally to this work. All the authors contributed to the discussions on the experimental and theoretical calculation results.

Additional information

Supplementary Information accompanies this paper at http://www.nature.com/naturecommunications.

Competing Interests: The authors declare no competing interests.

Figure 1.

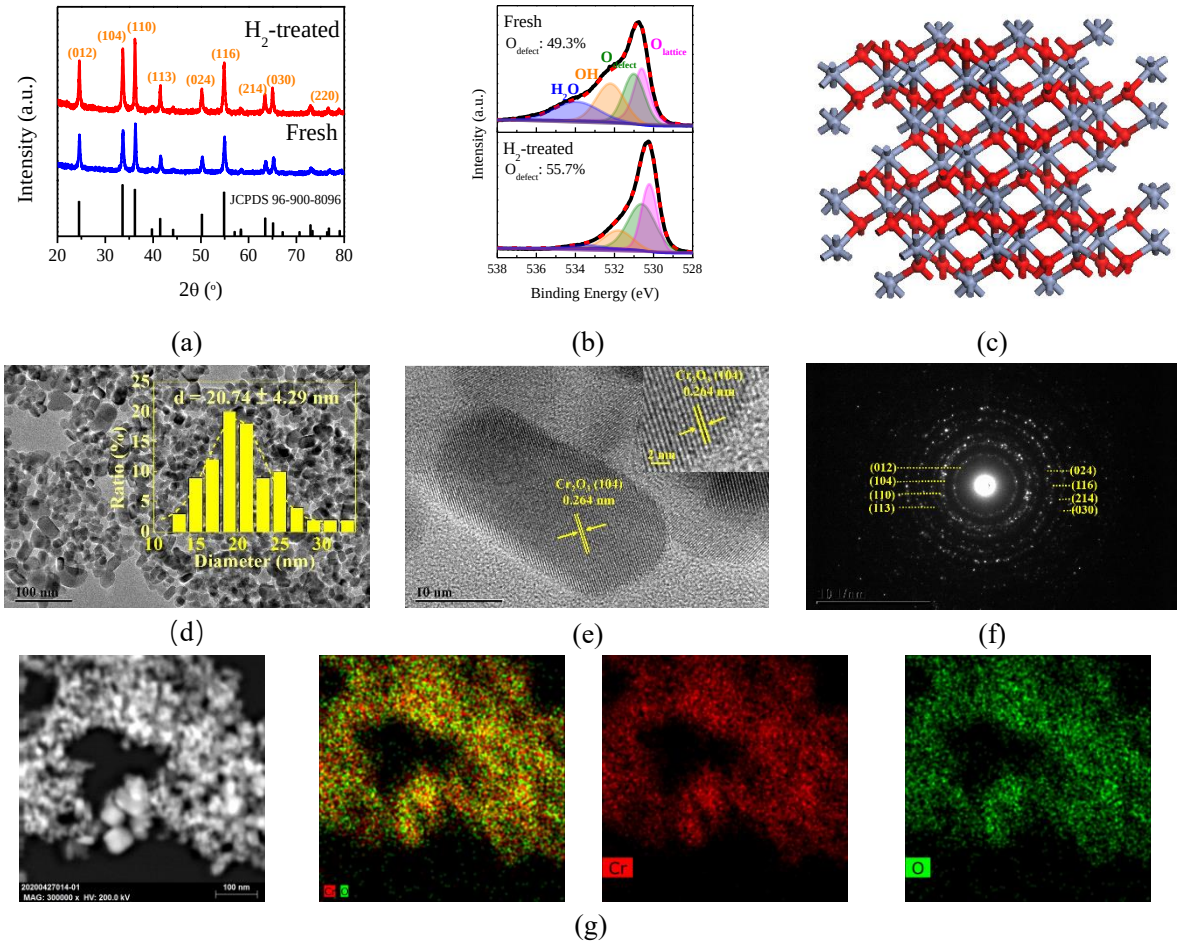

Figure 1. Catalysts characterization. (a) In situ XRD patterns and (b) in situ O(1s) XPS of fresh and H_2-treated (400 ºC for 2 h) Cr_2O_3; (c) crystal structure of hexagonal Cr_2O_3 (Cr: grey; O: red); (d) TEM image of Cr_2O_3 (Insert: particle size distribution estimated by counting 100 NPs); (e) HRTEM image of Cr_2O_3 (Insert: magnified images); (f) selected-area electron diffraction (SAED) patterns of Cr_2O_3; (g) HAADF-STEM image and EDX elemental distributions of Cr and O elements of Cr_2O_3.

Figure 2.

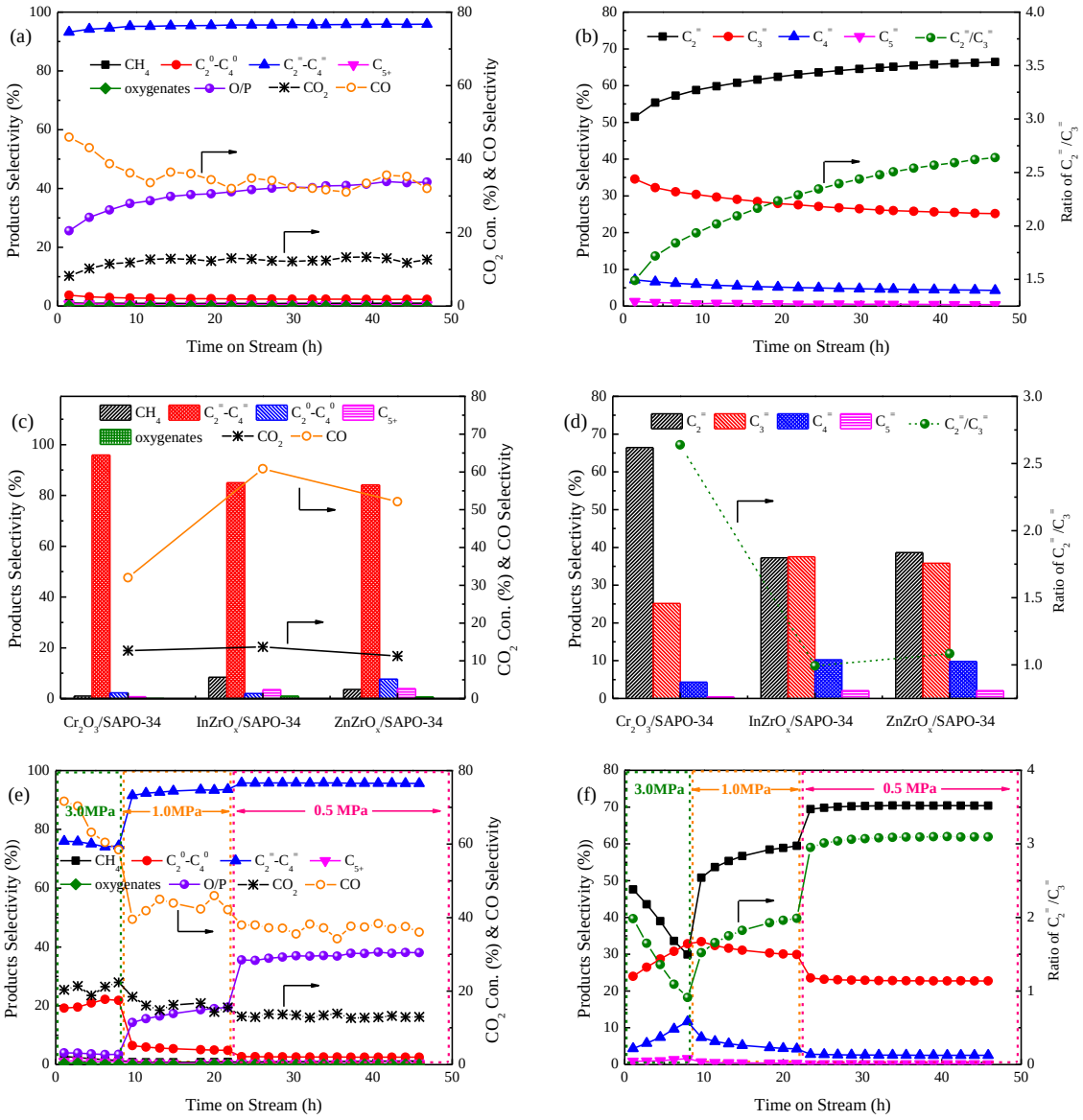

Figure 2. Catalytic results. Dependences of CO_2 conversion and product distribution on the reaction time ((a) and (b)) and the reaction pressure ((e) and (f)) on the Cr_2O_3/SAPO-34 composite catalyst; and CO_2 conversion and product distribution obtained over various metal oxides/SAPO-34 composite catalysts ((c) and (d)) (typical reaction conditions: H_2/CO_2 = 3:1, GHSV = 4000 mL/(g·h), 0.5 MPa and 370 °C).

Figure 3.

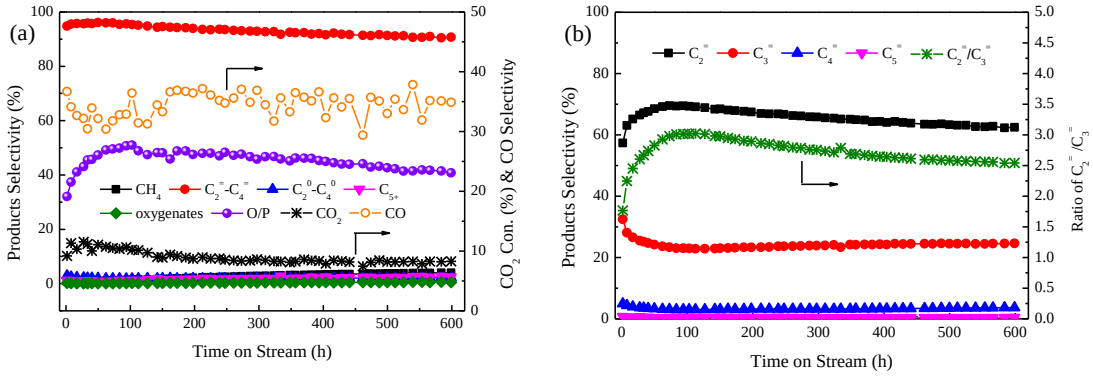

Figure 3. Catalyst stability. Catalytic stability of Cr_2O_3/SAPO-34 (Si/Al = 0.15) composite catalyst in CO_2 hydrogenation to light olefins (reaction conditions: H_2/CO_2 = 3/1, 370 °C, 0.5 MPa and GHSV = 4000 mL/g·h).

Figure 4.

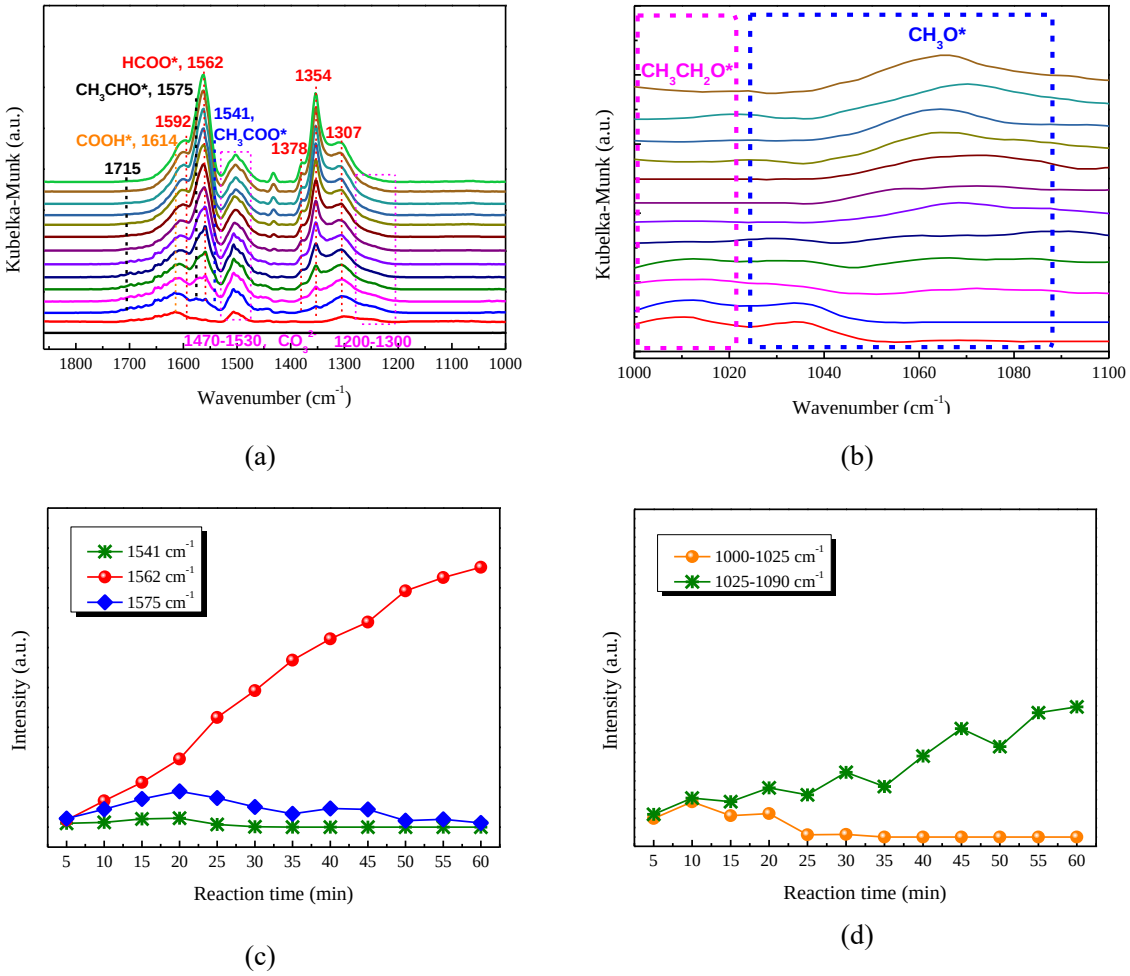

Figure 4. In situ DRIFT spectroscopy. (a) and (b) Time-dependent DRIFT spectra for CO_2 hydrogenation on neat Cr_2O_3 (the spectra were collected every 5 min up to 60 min after the sample was treated at 400 °C for 2 h in a H_2 flow (30 mL/min), and then, purged at 300 °C for 0.5 h with an Ar flow (30 mL/min) (typical reaction conditions: 300 °C, 0.1 MPa)); (c) and (d) evolutions of DRIFT peak intensity with the reaction time on neat Cr_2O_3 at 300 °C in CO_2 hydrogenation.

Figure 5.

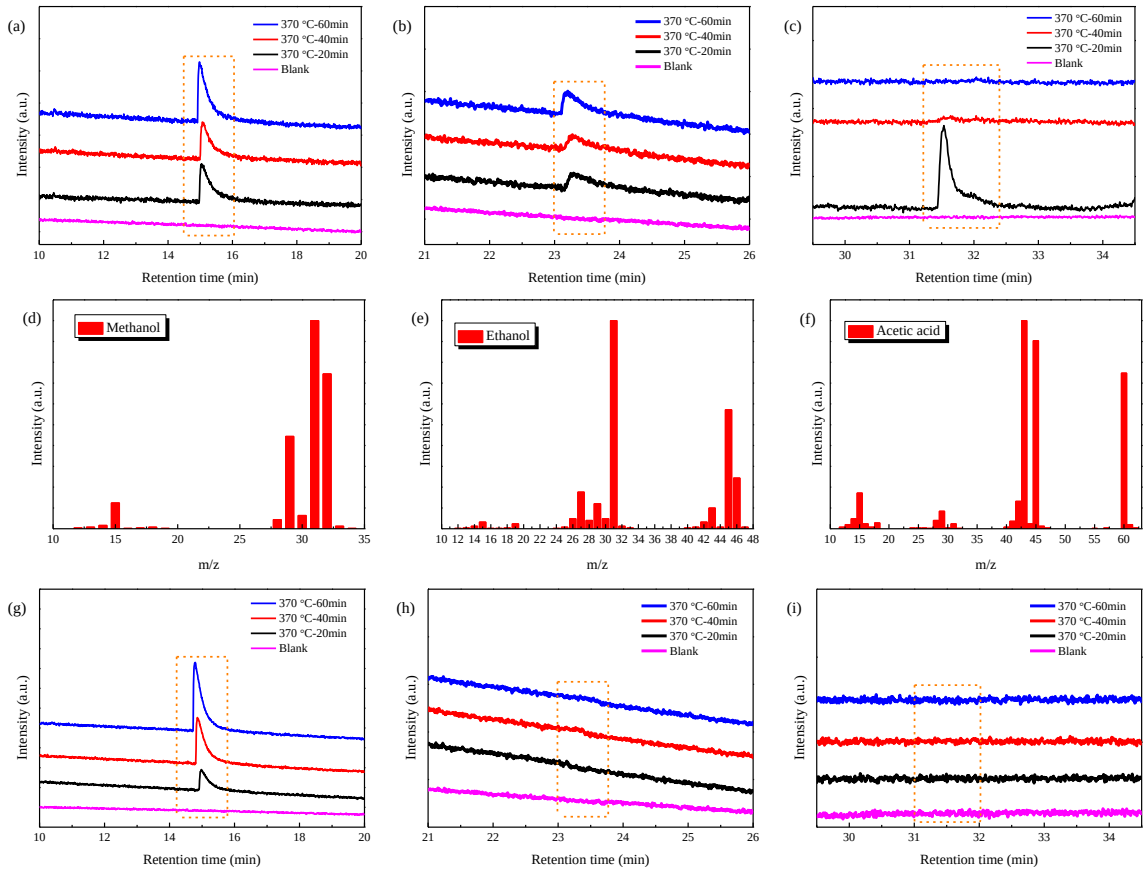

Figure 5. Reaction mechanism. GC-MS diagrams of the methanol ((a) and (g)), ethanol ((b) and (h)) and acetic acid ((c) and (i)) in effluents obtained at different times on neat Cr_2O_3 ((a), (b) and (c)) and $ZnZrO_x$ ((g), (h) and (i)) at 370 °C in CO_2 hydrogenation (typical reaction conditions: 370 °C and 0.5 MPa); corresponding MS spectra of the generated methanol (d), ethanol (e) and acetic acid (f) in effluents. The blank experiment was conducted under the same reaction conditions without using the catalyst.

Figure 6.

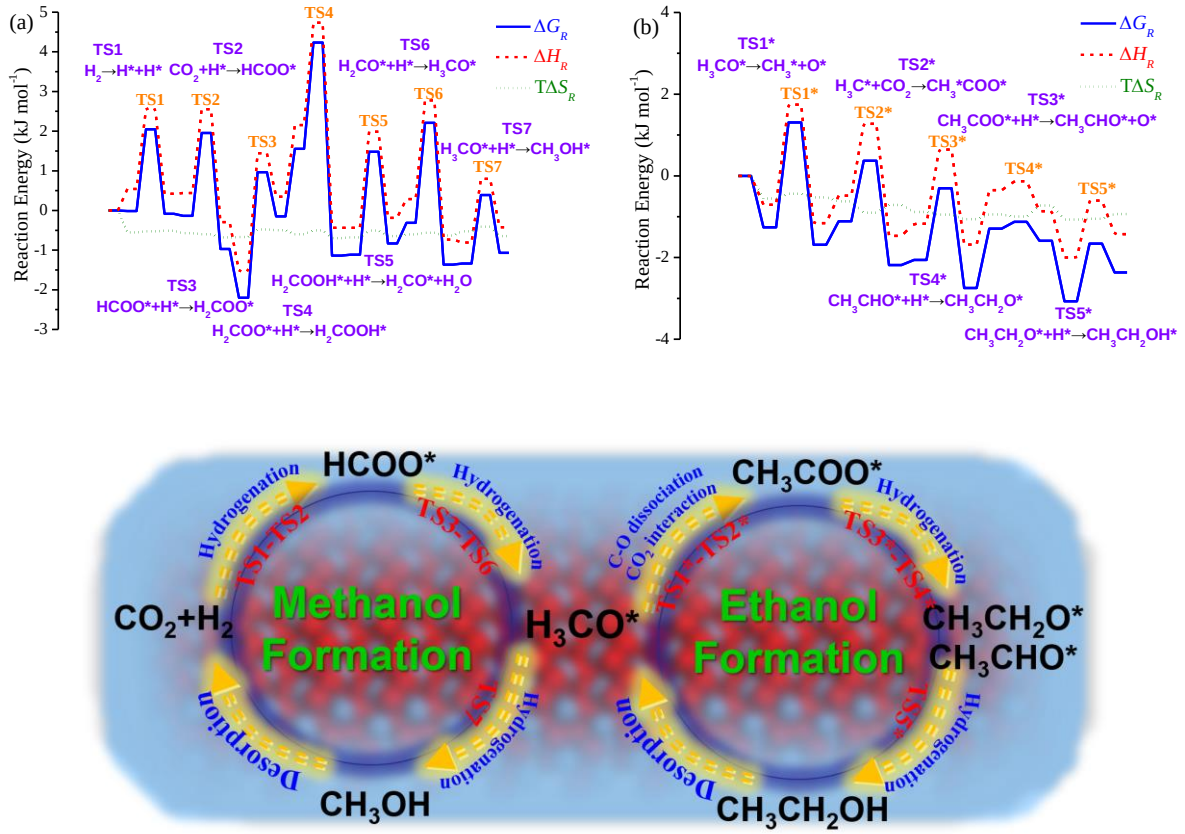

(c)

Figure 6. Density functional theory (DFT) calculations. (a) and (b) Free energy (ΔG_R), enthalpy (ΔH_R) and entropy ($T\Delta S_R$) profiles for CO_2 hydrogenation at 300 °C on Cr_2O_3; (c) reaction scheme for formation of methanol and ethanol in CO_2 hydrogenation on Cr_2O_3.